

## A multi-crystal wavelength dispersive x-ray spectrometer

Roberto Alonso-Mori,<sup>1</sup> Jan Kern,<sup>1,2</sup> Dimosthenis Sokaras,<sup>3</sup> Tsu-Chien Weng,<sup>3</sup> Dennis Nordlund,<sup>3</sup> Rosalie Tran,<sup>2</sup> Paul Montanez,<sup>1</sup> James Delor,<sup>1</sup> Vittal K. Yachandra,<sup>2</sup> Junko Yano,<sup>2</sup> and Uwe Bergmann<sup>1</sup>

<sup>1</sup>LCLS, SLAC National Accelerator Laboratory, Menlo Park, California 94025, USA

<sup>2</sup>Physical Biosciences Division, Lawrence Berkeley National Laboratory, Berkeley, California 94720-8099, USA

<sup>3</sup>SSRL, SLAC National Accelerator Laboratory, Menlo Park, California 94025, USA

(Received 10 May 2012; accepted 2 July 2012; published online 31 July 2012)

A multi-crystal wavelength dispersive hard x-ray spectrometer with high-energy resolution and large solid angle collection is described. The instrument is specifically designed for time-resolved applications of x-ray emission spectroscopy (XES) and x-ray Raman scattering (XRS) at X-ray Free Electron Lasers (XFEL) and synchrotron radiation facilities. It also simplifies resonant inelastic x-ray scattering (RIXS) studies of the whole 2d RIXS plane. The spectrometer is based on the Von Hamos geometry. This dispersive setup enables an XES or XRS spectrum to be measured in a single-shot mode, overcoming the scanning needs of the Rowland circle spectrometers. In conjunction with the XFEL temporal profile and high-flux, it is a powerful tool for studying the dynamics of time-dependent systems. Photo-induced processes and fast catalytic reaction kinetics, ranging from femtoseconds to milliseconds, will be resolvable in a wide array of systems circumventing radiation damage. © 2012 American Institute of Physics. [<http://dx.doi.org/10.1063/1.4737630>]

### I. INTRODUCTION

The development of X-ray Free Electron Lasers (XFELs) such as the linear coherent light source (LCLS) at SLAC National Accelerator Laboratory,<sup>1,2</sup> has allowed new opportunities to study the electronic and structural dynamics of a wide range of systems down to the femtosecond range. Light-induced catalysis, electron transfer, transient atomic or molecular states, chemical bond formation and dissociation, oscillation of atoms, and many other processes can be accessed by the ultra-short and ultra-bright x-ray pulses from the XFELs. Hard x-ray spectroscopies such as x-ray emission spectroscopy (XES) and x-ray Raman scattering (XRS), are unique element specific probes of the local electronic and atomic structure. XES offers elemental, structural, and spin selectivity of transition metal complexes via core-hole excitations,<sup>3</sup> and XRS is a powerful bulk sensitive probe of the bonding structure of low Z elements.<sup>4</sup> When combined with femtosecond XFEL pulses, these techniques can be used to study ultra-fast electronic structure dynamics in a wide variety of phenomena.

In the past few years, XES has proved to be a powerful technique when used with high brilliance x-ray photons with intensity and polarization tunability that modern synchrotron radiation sources offer. XES has been used to probe the electronic structure of a wide range of materials. In the soft x-ray regime, using grazing incidence angle grating spectrometers,<sup>5</sup> XES has attracted much attention for its unique capabilities to measure energetics, momentum, and spin in material science, mainly superconductors and transition metal oxides<sup>6,7</sup> and surface adsorbates.<sup>8</sup> Hard x-ray emission offers several practical advantages over soft x-ray emission, in particular for the sample environment and the use of Bragg crystals for detection, which has broadened the scope

and variety of samples that can be probed by XES to include, e.g., important enzymes,<sup>9–14</sup> catalytic systems under ambient conditions,<sup>15</sup> transition metal complexes,<sup>16–19</sup> and geochemical compounds.<sup>20–22</sup> More recently, XES has also been used to study the dynamics of time dependent systems with the limitation of the storage ring's temporal resolution of a few picoseconds.<sup>23</sup>

The most common spectrometers used for collecting the emission signal with a high-energy-resolution in the hard x-ray regime, are based on Bragg reflections from single or multiple perfect crystals in a Johann<sup>24</sup> or Johansson<sup>25</sup> geometry aligned on Rowland circles. In the paper by Stojanoff *et al.*<sup>26</sup> an early version of a single-crystal spectrometer is described. Various multi-crystal emission spectrometers, the majority based on the Rowland geometry, have been recently developed to enhance the capabilities of the technique regarding solid angle and therefore sensitivity and collection efficiency. The first of these multi-crystal instruments was developed by Wang *et al.*,<sup>27</sup> and a new design based on an 8-crystal analyzer spectrometer using a simpler scanning procedure was built by Bergmann and Cramer.<sup>28</sup> Several of these multi-crystal instruments are in operation nowadays at various synchrotron radiation facilities, for, e.g., ESRF (beamline ID26, 5 analyzers,<sup>29</sup> and beamline BM30B/CRG-FAME XAS, 5 analyzers<sup>30</sup>), SSRL (beamline 6-2, 7 analyzers coupled with two 40 and 14 analyzer Raman spectrometers),<sup>11,31</sup> SLS (beamline SuperXAS),<sup>32</sup> NSLS (beamline X21, 9 analyzers),<sup>33</sup> and ESRF. (Depending on the required energy resolution and sensitivity, systems currently employed vary in their focal lengths, analyzer size or crystal type (mostly Si or Ge.) Furthermore, the analyzers can be either spherically bent or diced.<sup>34</sup>

These spectrometers are very suitable for applications at synchrotron radiation sources, as they provide the best

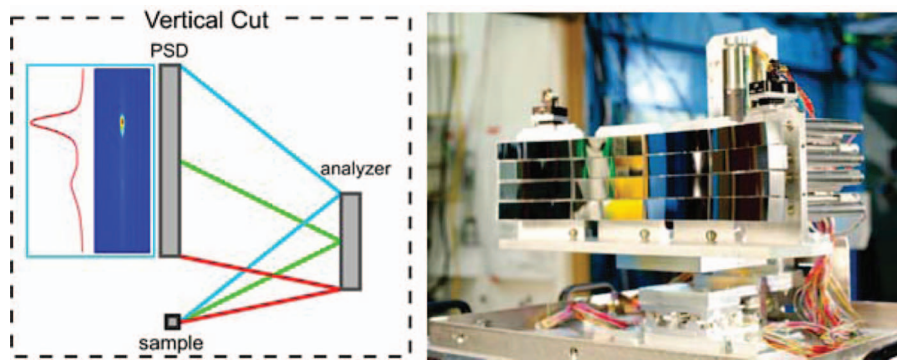


FIG. 1. Schematic view of a vertical cut of the Von Hamos geometry with a crystal analyzer and a position-sensitive detector (PSD). Scattering of a point source beam is analyzed at different energies resulting in an energy-dispersive spectrum on the PSD (left). The instrument showing the array of crystal analyzers (right, photo by M. Beardsley).

signal to background ratio due to their one-to-one focusing geometry. All of these systems have in common that an emission spectrum is obtained by scanning the instrument. The characteristics of the new XFELs make it desirable to have instrumentation that enables the spectrum acquisition on a single-shot basis. Dispersive x-ray emission spectrometers can be used to take shot-by-shot measurements, enabling the use of XES simultaneously with other techniques; i.e., x-ray diffraction (XRD) or scattering measurements. A dispersive setup can also facilitate the study of the two-dimensional energy plane (incident versus emitted/scattered energy) in RIXS studies,<sup>35</sup> as it eliminates the requirement to scan the photons-out spectrum. In recent years, several of the dispersive setups have been developed and applied. Some existing Rowland designs were adapted to achieve the wavelength dispersion by positioning the sample inside the Rowland circle and using a position-sensitive detector (PSD). A high-resolution single-crystal spectrometer of this kind is described elsewhere for tender x-ray applications.<sup>36</sup> A variation of the Rowland geometry, where many small flat crystals are placed on a spherically curved surface with radius of curvature of only a few centimeters, was employed to design a large solid angle x-ray spectrometer.<sup>37</sup> A different wavelength dispersive geometry, Von Hamos,<sup>38</sup> was also used to design shot-to-shot spectrometers.<sup>39,40</sup> Each of these designs has certain advantages and disadvantages including attainable solid angle, spectral width, energy resolution, sample geometry, and signal to background. The instrument described in this work is based on multiple-crystals in a wavelength dispersive Von Hamos geometry and is optimized to combine a large solid angle with sub eV energy-resolution covering a spectral width suitable for XES and near edge XRS, and is typically operated in the 5–10 keV region.

## II. DESIGN OF THE INSTRUMENT

A schematic of the Von Hamos geometry is shown in Fig. 1, left. The spectrometer is used at Bragg angles close to backscattering in order to optimize the solid angle per energy and the energy-resolution. The angle between the incident and emitted x-rays (scattering angle) is set to  $90^\circ$  to minimize the contribution of the unwanted elastic scattering from the sample (when linearly polarized photons are used). An ar-

ray of up to  $4 \times 4$  crystal analyzers diffracts and focuses the emitted radiation from the sample to a 2D detector following Bragg's law,  $n\lambda = 2d \sin \theta$ . The analyzers (manufactured by Saint-Gobain Cristaux et Détecteurs company), with a size of  $110 \times 25 \text{ mm}^2$  (horz x vert), are cylindrically bent with a radius of curvature of 500 mm perpendicular to the scattering plane. The RT4XES ray tracing code<sup>41</sup> was used to evaluate the performance of various dispersive geometries when the spectrometer was in the design phase. This code is also used to calculate the contributions to the energy broadening and the energy and intensity distributions when the spectrometer is set to different modes of operation.

The sample and detector are positioned on the axis of curvature of the crystal analyzers (see Fig. 1, right). The vertical position of the crystal array, relative to the sample, defines the Bragg angle and therefore the energy region of interest. The entire array is mounted on a stage with vertical and horizontal travel range of 40 mm, which allows the optimization of the signal and focus on the 2D detector. The curvature direction of the analyzers provides focusing, whereas the perpendicular direction gives the energy dispersion. For each crystal analyzer, integration along the focusing direction of the signal on the PSD results in an emission spectrum. The energy range of the spectrum is set by the height of the crystal analyzers, which defines the Bragg angle range. It has to be noted that the analyzers are not set perpendicular to the horizontal plane, as in the original Von Hamos geometry for a single analyzer (Fig. 1, left). According to their vertical position in the array, the analyzers are slightly tilted so they all diffract the same Bragg angles and therefore the same energy range. Figure 2 (left) shows the energy distribution as a function of the detector pixel position in the dispersive direction (in this case a Pilatus 100k detector, with pixel size  $172 \times 172 \mu\text{m}^2$ , was used). This curve is used for energy correction and calibration of the spectrometer.

Each individual crystal analyzer is equipped with three computer controlled motorized actuators, making it possible to individually align them. Two actuators are used for the angular alignment, pitch (to adjust the Bragg angle) and yaw (perpendicular to the Bragg angle direction). The third actuator results in a linear motion along the normal direction of the analyzer when used simultaneously with the other two. For applications where the signal to background needs to be

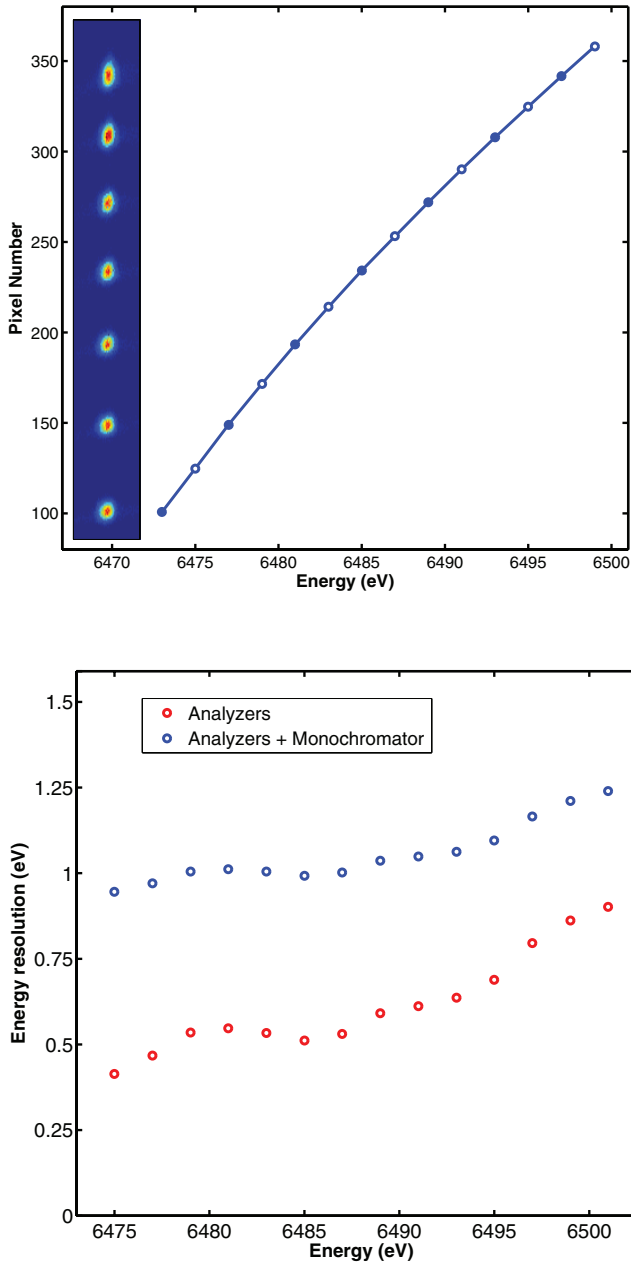


FIG. 2. (Top) Energy vs detector pixel position in the dispersive direction, the inset shows the elastic peak images corresponding to the filled line points. (Bottom) Energy resolution vs emission energy of the spectrometer with and without the contribution of the beamline monochromator for the Mn  $K\beta_{1,3}$  spectral range. Values were obtained from the elastic peaks around the Mn  $K\beta$  energy with 16 Si(440) analyzers.

maximized, all analyzers are lined up on to one column of the PSD.

The achievable energy resolution of the instrument includes major geometrical contributions ( $\Delta E_G$ ), and the intrinsic energy resolution ( $\Delta E_{int}$ ). The  $\Delta E_{int}$  has two main components, the Darwin width, and the broadening associated with the stress induced in the lattice planes when the analyzer is bent. The last is estimated, for 0.5 m cylindrically bent crystal analyzers in the Si(440) reflection, to be  $\Delta E_S \cong 0.15$  eV.<sup>42</sup> The Darwin width of a perfect crystal Bragg reflection,  $\Delta E_D$ , can be calculated from dynamical diffraction theory.<sup>43,44</sup> For Si(440) reflection, at an incident energy of 6490 eV (angle),

the Darwin width is  $\Delta E_D = 0.065$  eV. In most general terms, the geometrical contributions are described by a derivative of Bragg's law as

$$\frac{\Delta E_G}{E} = \Delta \theta_G \cot \theta, \quad (1)$$

where  $E$  is the incident x-ray energy,  $\theta$  is the Bragg angle, and  $\Delta \theta_G$  summarizes any angular deviation from the exact Bragg condition. For this type of dispersive optics the major contribution to this angular deviation is given by  $\Delta \theta \cong (s+d)/f$ ,<sup>45</sup> where  $s$  is the vertical beam size,  $d$  is the detector spatial resolution, and  $f$  is the analyzer-detector distance. Note that in the Von Hamos geometry, unlike in the Rowland geometry based on Johann crystals, Johann aberrations<sup>28</sup> do not degrade the energy resolution. With a detector pixel size of 0.172 mm and a vertical beam size of 0.1 mm, for  $\theta = 84.2^\circ$  at 6490 eV incident energy, the resulting energy broadening due to geometrical contributions is  $\Delta E_G \cong 0.36$  eV.

The use of crystals on multiple rows (see Fig. 1) results in an additional contribution to the energy resolution. Analyzers in different rows are slightly tilted in theta, to fulfill the same Bragg angles, leading to a small spread of energies. In addition, errors in the alignment of the 16 crystals and variations in the crystal quality may also contribute to the energy resolution. We estimate these contributions,  $\Delta E_M$ , to produce  $\cong 0.20$  eV broadening. Accounting all the contributions discussed above we obtain

$$\begin{aligned} \Delta E_{tot} &= (\Delta \theta_G^2 + \Delta \theta_D^2 + \Delta \theta_S^2 + \Delta \theta_M^2)^{1/2} \\ &= (0.36^2 + 0.065^2 + 0.15^2 + 0.20^2)^{1/2} \\ &= 0.44 \text{ eV}. \end{aligned} \quad (2)$$

In a standard synchrotron-based experiment, using monochromatic incident x-rays, the Darwin width of the monochromator crystals has to be also taken into account. The total resolution is then the convolution of the spectrometer and monochromator contributions (0.86 eV for Si(111) and 0.25 eV for Si(311) at 9000 eV). For the study of Mn  $K\beta$  XES ( $\sim 6490$  eV), 16 Si(440) analyzers were installed at SSRL beamline 6-2 (see Sec. III for beamline specifications). In this setting, an instrumental energy resolution of  $\Delta E \cong 0.55$  eV was achieved at 6490 eV after deconvoluting the Si(111) monochromator contribution to the elastic scattering peak (Fig. 2, right).

The total solid angle (SA) of the spectrometer when used in full range is 1.3% of  $4\pi$  (165.6 msr), resulting in  $\sim 0.04\%$  of  $4\pi$  (5.4 msr) per 1 eV (on average) for the energy of Mn  $K\beta$  (6490 eV, using 16 Si(440) crystals). For any given configuration the average SA per 1 eV is given by

$$SA_{1 \text{ eV}} \cong SA/E_{range}, \quad (3)$$

where the SA depends on the number of crystals ( $n$ ), crystals height and width ( $a$  and  $b$ ), the radius of curvature ( $R$ ), and the Bragg angle ( $\theta$ ). The energy range is defined by the Bragg angle projected by the crystal analyzers height ( $a$ ), and it can then be calculated as follows:

$$SA = \left( \frac{n \times a \times b}{R^2} \right) (\sin \theta), \quad (4)$$

$$E_{range} = E_{top} - E_{bot}, \quad (5)$$

$$E_{[top, bot]} \cong \frac{c \times h}{2d \sin \left( \arctan \left( \frac{R}{\frac{R}{\tan \theta} \left[ \begin{smallmatrix} + \\ - \end{smallmatrix} \right] \frac{a}{2}} \right) \right)}, \quad (6)$$

where  $d$  is the  $d$ -spacing of the crystals,  $c$  is the speed of light, and  $h$  is the Planck's constant. For comparison, a standard 100 mm diameter spherically bent crystal analyzer working on a 1 m scanning Rowland geometry, covers a SA of  $\sim 7.9$  msr (for Bragg angles close to  $90^\circ$ ). This value is within the same order of magnitude as the SA per 1 eV of the Von Hamos spectrometer. However, the advantage of the dispersive setup lies in the simultaneous collection of the whole energy range, and effectively the total SA should be compared for both geometries. Note that the solid angle per 1 eV in the Von Hamos geometry is strongly dependent on the Bragg angle (Eq. 6), whereas in the Rowland geometry there is a much weaker dependence.<sup>28</sup>

The spectrometer can be used in different configurations. Different crystals can be aligned at different positions depending on the application. This makes it possible to focus crystals of different array columns at different positions of the detector for polarization studies (each crystal covers  $12.4^\circ$ ), see Fig. 3. The deviation of the individual crystals' energy resolution, due to their position in the array, is less than 10%. This difference is mainly dominated by variations in crystal quality. As seen in Fig. 3, spectra collected with different columns look alike, allowing the use of different units of the crystal array to be used simultaneously to collect the emission signal. The difference in energy resolution between the different columns is  $\sim 4\%$  ( $\sim 3\%$  for the difference between rows).

The spectrometer is a stand-alone, compact, and portable system, making it possible to be installed in any x-ray source. All components used to build the spectrometer are vacuum compatible, allowing the use of the instrument for both, in-air and in-vacuum applications.

The main advantages associated with the use of the Von Hamos geometry result from the capability to take an spectrum with no need of scanning, e.g., simpler and more robust mechanics and high stability since there are no moving parts; elimination of the dead time associated with the scanning movements; possible artifacts produced by the imperfect synchronization of the various moving elements during the scanning process are eliminated; an easy crystal alignment procedure is achieved since the diffracted signal is monitored by a 2D detector and the spectra can be taken in a single shot mode on an XFEL. This geometry is particularly suited for time-resolved measurements such as pump-probe experiments, as it eliminates errors from spectrum normalization. The geometry is further convenient when collecting 2D RIXS spectra, since only the incident energy is scanned, which simplifies the data collection. An additional advantage is derived from the use of cylindrically bent crystals, since the strain produced in the lattice plains is smaller as compared to spherically bent crystals.<sup>42</sup> This results in a better intrinsic energy resolution for the same radius of curvature and makes

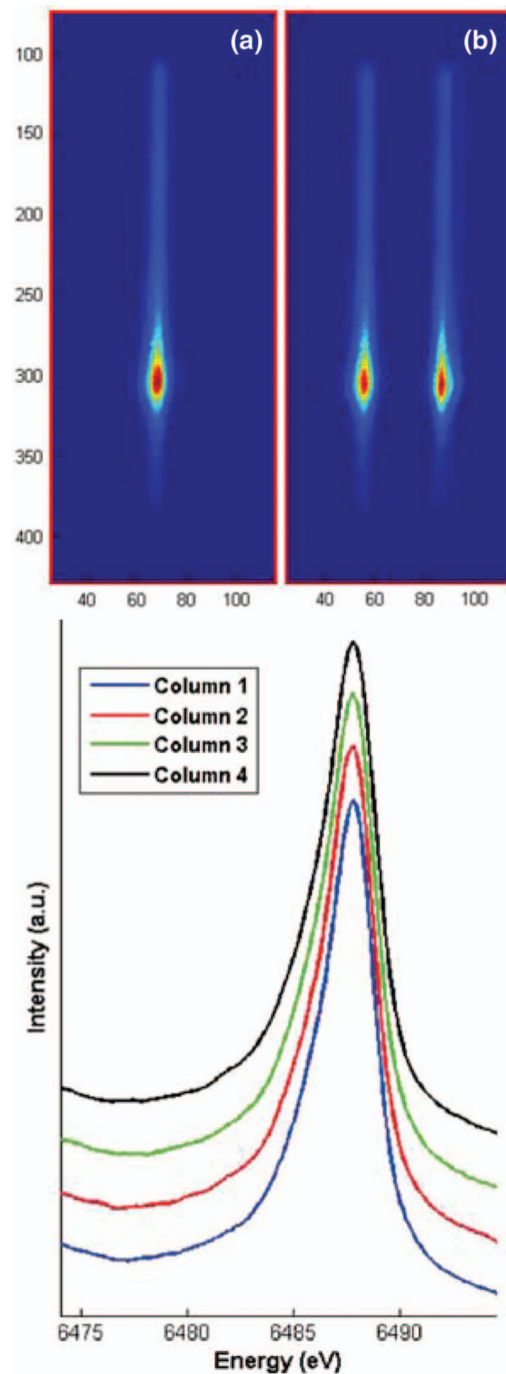


FIG. 3. (Top) Image of  $\text{Mn}_2\text{O}_3$  emission with all the crystals focused on one line (a) and with columns 1-2 and 3-4 focused in different lines (b). Mn  $K\beta_{1,3}$  peak from  $\text{Mn}_2\text{O}_3$  collected by the 4 columns of the spectrometer individually.

it possible to design spectrometers with much smaller radius of curvature and significantly larger solid angles. The easier bending process also results in significant costs reduction. A further improvement of the solid angle as compared to the Rowland geometry is obtained by the use of a large number of crystals without significantly losing performance (resolution or energy distributions). Finally, as mentioned before, the use of multiple crystals gives the freedom to choose between different alignment schemes, so polarized information can be gathered (alignment by columns) or different elements



can be measured simultaneously (alignment by rows with different crystal reflections). The use of a dispersive geometry can help avoiding the inherent problems caused by inhomogeneities of the sample, particularly when using a liquid jet for sample injection, or when scanning through the sample becomes necessary, like for samples that are very sensitive to radiation damage.<sup>46</sup>

Von Hamos spectrometers collect all the solid angle into an extended area in contrast to the Rowland approach where all the solid angle is collected into one point. Therefore, the signal to background ratio is lower when compared with the one obtained in a Rowland based spectrometer. Another disadvantage of using dispersive optics is the possibility of introducing artifacts in the spectrum produced by defects in the quality of the crystals. Furthermore in any dispersive Bragg optics, the solid angle covered per analyzer is proportional to the corresponding spectral width, unlike in the Rowland geometry, this requires a different vertical analyzer size for different spectral ranges of interest. This is particularly relevant for spectrometers that require small spectral range but are operated away from backscattering, since the solid angle per eV achievable per crystal is limited. In addition, a small x-ray beam size is required to optimize the energy resolution of the measurements as shown above.

As in any dispersive setup, a two-dimensional detector is required to collect the signal for spectrometers based on the Von Hamos geometry. In order to cover the whole spectral range, the detector active area is required to be twice the height of the crystal analyzers, which is chosen to match the energy range of the emission lines of interest. Small detector pixel size is also convenient for several reasons. The better spatial resolution obtained with smaller pixels is directly translated into better energy resolution. It also allows the binning of multiple pixels to obtain the desired energy points in the spectrum enhancing the efficiency of the collection. As an example, collecting Fe K $\beta$  spectra (7057 eV) by a detector with 110  $\mu\text{m}^2$  pixel size, results in an energy range of 0.14 eV collected per pixel. Therefore, 7 pixels could be binned together to obtain an energy separation of 1 eV and higher count rates.

### III. APPLICATIONS

The spectrometer was commissioned at the wiggler beamline 6-2 at Stanford Synchrotron Radiation Lightsource (SSRL). The monochromator on the beamline, which uses two liquid nitrogen cooled Si crystals in the (111) reflection, was used to set the incident photon energy to 9 keV. The x-ray beam was focused to  $\sim 500 \times 150 \mu\text{m}^2$  (horz x vert) by means of a parabolic Rh-coated mirror. The fundamental of the monochromator gives, at 9 keV, a total flux of  $\sim 1.5 \times 10^{13}$  photons/s at a ring current of 350 mA. A Pilatus 100 K detector with an active area of  $84 \times 34 \text{ mm}^2$  and pixel size of  $172 \mu\text{m}^2$  was used to collect the emission signal. The monochromator energy was calibrated to the  $\text{KMnO}_4$  pre-edge peak (6543.3 eV) for Mn and to the first derivative of the Fe edge from a metallic Fe foil (7112.0 eV) for Fe. The elastic scattering peak was recorded for several incident energies to calibrate the spectrometer (see Fig. 2, left). A 1 mil (25  $\mu\text{m}$ )

thick polypropylene balloon filled with helium was installed between the sample, the spectrometer, and the detector in order to avoid the strong absorption by air in this energy regime (11% vs 99% transmission for 6500 eV photons through 1 m of air and helium, respectively).

#### A. Mn K $\beta$ XES

A set of 16 Si(440) crystal analyzers was used to record Mn K $\beta$  XES. The Bragg angle range was set from  $85.9^\circ$  to  $82.9^\circ$ , corresponding to an energy range from 6473.7 to 6506.3 eV (given by the height of each crystal, 25 mm). The 32.6 eV covered by the spectrometer are distributed over a 50 mm area on the detector and each of the Pilatus 100 k pixels collects an average of  $\sim 0.11$  eV. The height of the center of the analyzer array and the detector with respect to the sample was 50.8 mm and 101.6 mm, respectively. The energy resolution of the spectrometer in this configuration is 0.55 eV at 6490 eV, after deconvoluting the Si(111) mono contribution. A count rate of 2000 counts/s was obtained from a thick pellet of MnO at the maximum of the Mn K $\beta_{1,3}$  peak ( $\sim 125\,000$  c/s in the whole spectral area), and thus, sufficient statistics were obtained after an acquisition time of a few seconds for each spectrum. These count rates should be sufficient to allow the collection of a spectrum at an XFEL after integrating the signal obtained by several pulses (assuming  $\sim 10^{12}$  photons per pulse) in a reasonable time, even for diluted samples.

In Fig. 4, the K $\beta_{1,3}$  spectra of two different manganese oxides ( $\text{Mn}^{\text{IV}}\text{O}_2$  and  $\text{Mn}^{\text{II}}\text{O}$ ) are shown. The Mn K $\beta$  emission lines are produced by the transition between the 3p and the 1s core levels. We can observe a significant shift in the main peak produced by the screening effect on the 3p orbitals by the different valence shell occupancy and also the 3p-3d exchange interaction coupling in Mn(II) and Mn(IV). We can

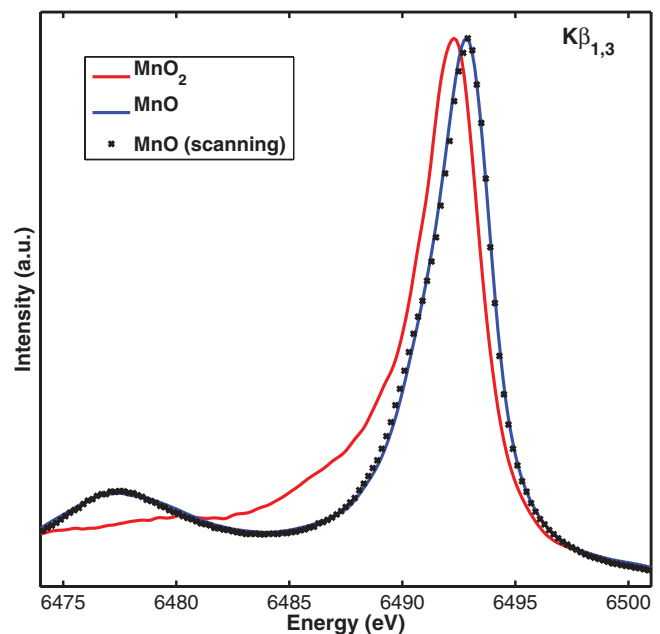


FIG. 4. Mn K $\beta_{1,3}$  spectra of  $\text{Mn}^{\text{IV}}\text{O}_2$  and  $\text{Mn}^{\text{II}}\text{O}$ . Integration time 100 s. A second spectrum from  $\text{Mn}^{\text{II}}\text{O}$  collected by means of an scanning spectrometer is also shown for comparison.

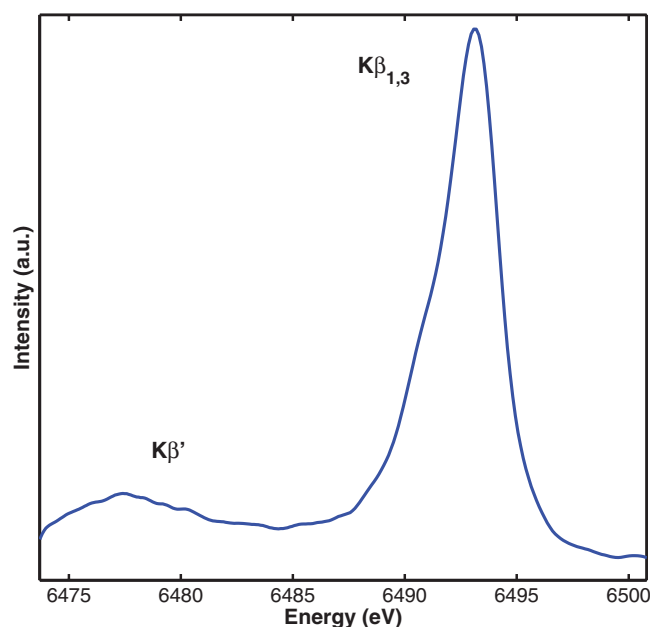


FIG. 5. Mn  $K\beta_{1,3}$  spectra of Mn in PS II solution (0.8 mM Mn concentration). Integration time 30 min. Note that the spectrum is that of fully photoreduced Mn in PSII.

also observe the characteristic  $K\beta'$  peak in the lower energy part of the spectra.

For comparison, the spectrum of  $Mn^{II}O$  previously recorded by means of a scanning Rowland geometry based spectrometer is shown as a black dotted line in Fig. 4. The spectra collected from both, dispersive and scanning geometries are alike.

The  $K\beta_{1,3}$  spectrum of Mn recorded from the membrane bound protein, Photosystem II (PS II) is shown in Fig. 5. The Mn concentration in this sample was about 0.8 mM and the sample was exposed to the 9 keV x-rays at room temperature for 2000 s. Although under these conditions all Mn in the sample is reduced from the native Mn(III) and Mn(IV) to Mn(II), the spectrum can be used to estimate the required measurement time to obtain an undamaged spectrum from this radiation sensitive enzyme using a large number of sample spots and a short exposure time for each spot. We obtained a count rate of 200 counts/s at the  $K\beta_{1,3}$  peak. The signal to background is  $\sim 4$ , which can be improved to  $\sim 9$  by utilizing a 25  $\mu m$  Fe filter in front of the detector to reduce the signal from the incident scattering photons (9000 eV).

A Mn  $K\beta_{2,5}$  spectrum (valence-to-core transitions) of  $Mn^{IV}O_2$  was also recorded using the Si(440) crystal analyzers (see Fig. 6). The Bragg angle range was set from  $82.7^\circ$  to  $79.8^\circ$ , corresponding to an energy range from 6510.6 eV to 6560.6 eV. The 50 eV covered by the spectrometer are distributed over a 50 mm area on the detector and each of the Pilatus 100 k pixels collected an average of  $\sim 0.17$  eV. The crystal array and detector were set to a height of 78.3 and 156.6 mm, respectively, from the sample. The Mn  $K\beta_{2,5}$  emission lines directly probe the valence orbital population. The crossover peak or  $K\beta''$  emission line is also shown around 6518 eV. A count rate of 550 counts/s was obtained for  $Mn^{IV}O_2$  at the Mn  $K\beta_{2,5}$  peak.

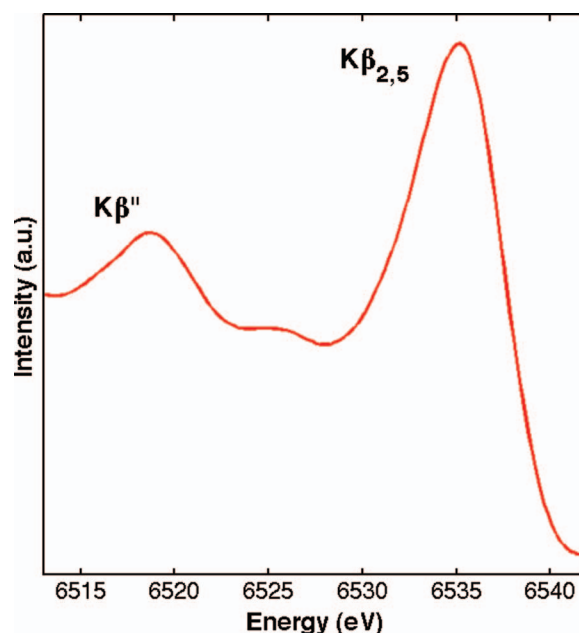


FIG. 6. Mn  $K\beta_{2,5}$  spectrum of  $Mn^{IV}O_2$  with an integration time of 30 min.

## B. Fe $K\beta$ XES

The first row of the spectrometer crystal array, populated by 4 Ge(620) crystal analyzers, was used to record Fe  $K\beta_{1,3}$  emission spectra of  $Fe^{II}O$  and  $Fe_2^{III}O_3$  (see Fig. 7). The Bragg angle range was set from  $80.47^\circ$  to  $77.69^\circ$ , corresponding to an energy range from 7027 to 7093 eV. The 66 eV covered by the spectrometer are distributed over a 50 mm area on the detector and each of the Pilatus 100 k pixels collected an average of 0.22 eV. The height of the center of the crystal row and the detector with respect to sample was 97.2 mm and 194.4 mm, respectively. The energy resolution of the spectrometer in this configuration is 0.52 eV at 7060 eV, after deconvoluting the Si(111) mono contribution. A count rate of 25 000 counts/s was obtained from a thick pellet of  $Fe^{II}O$  at the maximum of the Fe  $K\beta_{1,3}$  peak, and thus, sufficient statistics were obtained after an acquisition time of a few seconds for each spectrum.

## C. X-ray Raman spectra

X-ray Raman spectroscopy can be used to obtain information on the unoccupied electronic density similar to that obtained by means of soft x-ray absorption spectroscopy (XAS).<sup>4,47–55</sup> A spectrum, equivalent to an absorption spectrum, is obtained with non-dispersive Rowland-based spectrometers by scanning the energy of the hard-x-ray beam while analyzers collect the energy transfer. In this way some of the constraints associated with soft x-rays can be overcome, especially those derived from the strong absorption by matter limiting one to probe only the surface. For example, hard x-ray experiments probe the bulk and do not necessarily need to be performed under vacuum conditions, resulting in an easier setup and simpler sample change procedure. Also, high-pressure/temperature experiments become possible since the high-energy photons can pass through diamond anvil cells and various *in situ* cells. A further advantage of this approach

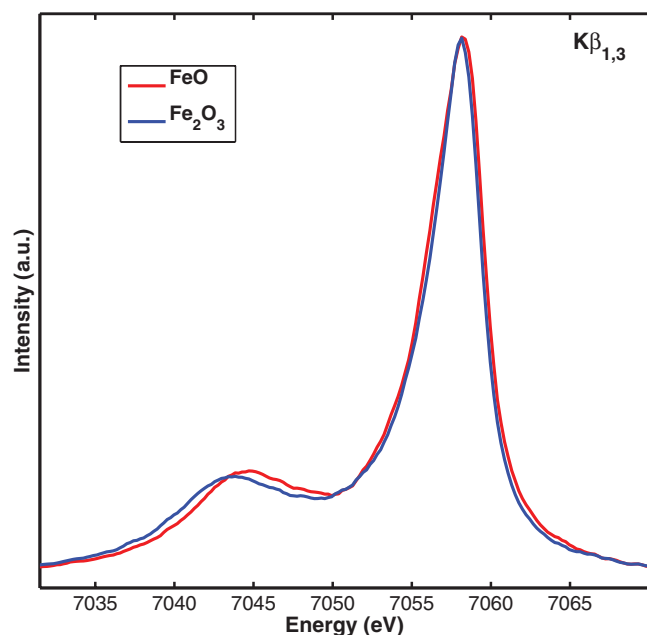


FIG. 7. Fe  $K\beta_{1,3}$  spectra from  $\text{Fe}^{\text{II}}\text{O}$  and  $\text{Fe}_2^{\text{III}}\text{O}_3$  with an integration time of 25 s.

is that the radiation dose deposited into the sample is much lower than that from soft x-rays for the same number of photons. This becomes especially important in biological samples sensitive to radiation damage.<sup>46</sup>

XRS is a very low cross section technique ( $\sim$ barns) and thus, the instrumentation requires a large solid angle and also a high resolution, similar to the one obtained by soft x-ray based techniques. Figure 8 shows the Carbon 1s edge of highly oriented pyrolytic graphite (HOPG) collected using 16 Si(440) crystal analyzers. The monochromator energy was set to 6780 eV. The Bragg angle range was set from  $86.5^\circ$  to  $83.3^\circ$ , corresponding to an analyzed energy range from 6468.7 to 6501.3 eV or an energy transfer range from 278.7 to 311.3 eV. The 32.6 eV covered by the spectrometer are distributed over a 50 mm area on the detector and each of the Pilatus 100 k pixels collects  $\sim 0.11$  eV. The spectrometer was

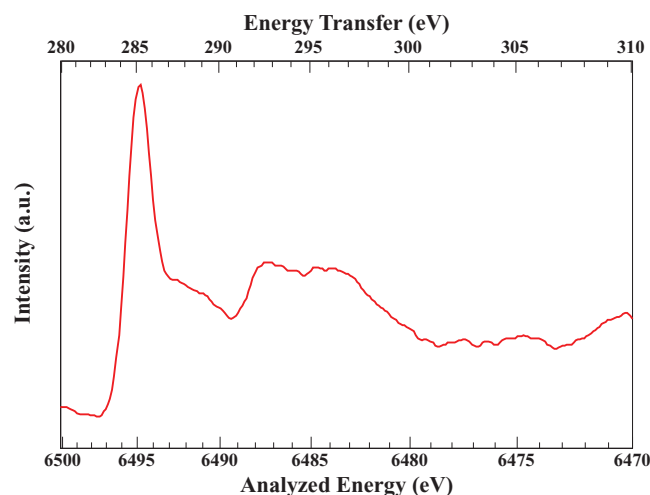


FIG. 8. C K-edge XRS spectrum of HOPG. Integration time was 30 min.

set to  $90^\circ$  with respect to the incident beam and in the polarization plane of the x-ray beam. The sample orientation was set to  $45^\circ$  with respect to the incident x-rays. The height of the center of the analyzer array and the detector with respect to the sample was 50.8 mm and 101.6 mm, respectively. The spectrum is in overall agreement with previous data collected by a Rowland geometry based Raman spectrometer.<sup>31</sup> This demonstrates the feasibility of using the dispersive instrument for XRS-based measurements.

#### IV. CONCLUSIONS

A wavelength dispersive x-ray spectrometer with capacity to computer control an array of up to  $4 \times 4$  cylindrically bent crystal analyzers is described. This portable spectrometer is operated with a two-dimensional PSD to collect hard x-ray photon-in photon-out spectra at synchrotron radiation facilities as well as at XFEL sources. It has a large collection angle (up to 170 msr) and high-energy-resolution ( $\sim 0.5$  eV at 6480 eV using Si(440)). Given these parameters, the study of very dilute biological systems and/or very weak emission and scattering signals using techniques such as XES, XRS, and RIXS is possible. Further, any set or combinations of sets of crystals can be employed, individually or simultaneously.

The instrument is suited to run in shot-by-shot mode where the samples are probed with the ultra-bright and ultrafast pulses from XFEL beams. It is particularly suited to be combined with other techniques, such as XRD or various scattering methods, to monitor the electronic structure and obtaining simultaneously both electronic and structural information. Such combinations might prove valuable for a large range of future XFEL-based studies.

#### ACKNOWLEDGMENTS

This research was carried out at the LCLS and SSRL, Directorates of SLAC National Accelerator Laboratory and Office of Science User Facility operated for the U.S. Department of Energy Office of Science by Stanford University. Financial support from the National Institutes of Health (NIH), National Institute of General Medical Sciences (NIGMS) (including P41GM103393) and the National Center for Research Resources (NCRR) (P41RR001209) (K. O. Hodgson; B. Hedman) is greatly acknowledged. The contents of this paper are solely the responsibility of the authors and do not necessarily represent the official views of NIGMS, NCRR or NIH. This work was also supported by the National Science Foundation (NSF) under Contract No. CHE-0809324 (A. Nilsson), the Alexander von Humboldt Foundation (J.K.) and by the AMOS program within the Chemical Sciences division of the Office of Basic Energy Sciences, Office of Science, U.S. Department of Energy (DOE) (K. Gaffney). Support by the Director, Office of Science, Office of Basic Energy Sciences, Division of Chemical Sciences, Geosciences, and Biosciences (CSGB) of the DOE under Contract No. DE-AC02-05CH11231 (J.Y. and V.K.Y.) for x-ray spectroscopy instrumentation development, NIH Grant No. GM

55302 (V.K.Y.), for Mn inorganic chemistry is acknowledged. In addition, we thank P. Glatzel, M. Kavčič, G. Vanko, and H. Hayashi for the discussions on the advantages and disadvantages of the different geometries. B. Plummer and M. Beardsley for photographic work. N. Kelez for efforts in the technical design and development of the project. M. Latimer, V. Borzenets, A. Garachtchenko, and the SSRL support group for the help with the test and commissioning beamtimes at SSRL beamlines 9-3, 10-2, 9-1, and 6-2, and P. Zwart, S. Morton, and B. Lassalle for help with commissioning beamtimes at ALS beamline 5.0.2.

- <sup>1</sup>J. Arthur, G. Materlik, R. Tatchyn, and H. Winick, "The LCLS - A 4th-generation light-source using the SLAC linac," *Rev. Sci. Instrum.* **66**(2), 1987–1989 (1995).
- <sup>2</sup>P. Emma, R. Akre, J. Arthur, R. Bionta, C. Bostedt, J. Bozek, A. Brachmann, P. Bucksbaum, R. Coffee, F. J. Decker, Y. Ding, D. Dowell, S. Edstrom, A. Fisher, J. Frisch, S. Gilevich, J. Hastings, G. Hays, P. Hering, Z. Huang, R. Iverson, H. Loos, M. Messerschmidt, A. Miahnahri, S. Moeller, H. D. Nuhn, G. Pile, D. Ratner, J. Rzepiela, D. Schultz, T. Smith, P. Stefan, H. Tompkins, J. Turner, J. Welch, W. White, J. Wu, G. Yocky, and J. Galayda, "First lasing and operation of an angstrom-wavelength free-electron laser," *Nat. Photonics* **4**(9), 641–647 (2010).
- <sup>3</sup>P. Glatzel and U. Bergmann, "High resolution 1s core hole x-ray spectroscopy in 3d transition metal complexes - electronic and structural information," *Coord. Chem. Rev.* **249**(1–2), 65–95 (2005).
- <sup>4</sup>U. Bergmann, P. Glatzel, and S. P. Cramer, "Bulk-sensitive XAS characterization of light elements: From x-ray Raman scattering to x-ray Raman spectroscopy," *Microchem. J.* **71**(2–3), 221–230 (2002).
- <sup>5</sup>J. Nordgren, G. Bray, S. Cramm, R. Nyholm, J. E. Rubensson, and N. Wassdahl, "Soft-x-ray emission-spectroscopy using monochromatized synchrotron radiation," *Rev. Sci. Instrum.* **60**(7), 1690–1696 (1989).
- <sup>6</sup>A. Kotani and S. Shin, "Resonant inelastic x-ray scattering spectra for electrons in solids," *Rev. Mod. Phys.* **73**(1), 203–246 (2001).
- <sup>7</sup>L. J. P. Ament, M. van Veenendaal, T. P. Devereaux, J. P. Hill, and J. van den Brink, "Resonant inelastic x-ray scattering studies of elementary excitations," *Rev. Mod. Phys.* **83**(2), 705–767 (2011).
- <sup>8</sup>A. Nilsson and L. G. M. Pettersson, "Chemical bonding on surfaces probed by x-ray emission spectroscopy and density functional theory," *Surf. Sci. Rep.* **55**(2–5), 49–167 (2004).
- <sup>9</sup>U. Bergmann and P. Glatzel, "X-ray emission spectroscopy," *Photosynth. Res.* **102**(2–3), 255–266 (2009).
- <sup>10</sup>J. Messinger, J. H. Robblee, U. Bergmann, C. Fernandez, P. Glatzel, H. Visser, R. M. Cinco, K. L. McFarlane, E. Bellacchio, S. A. Pizarro, S. P. Cramer, K. Sauer, M. P. Klein, and V. K. Yachandra, "Absence of Mn-centered oxidation in the S<sub>2</sub> > S<sub>3</sub> transition: Implications for the mechanism of photosynthetic water oxidation," *J. Am. Chem. Soc.* **123**(32), 7804–7820 (2001).
- <sup>11</sup>J. Pushkar, X. Long, P. Glatzel, G. W. Brudvig, G. C. Dismukes, T. J. Collins, V. K. Yachandra, J. Yano, and U. Bergmann, "Direct detection of oxygen ligation to the Mn<sub>4</sub>Ca cluster of photosystem II by x-ray emission spectroscopy," *Angew. Chem., Int. Ed.* **49**(4), 800–803 (2010).
- <sup>12</sup>K. M. Lancaster, M. Roemelt, P. Ettenhuber, Y. L. Hu, M. W. Ribbe, F. Neese, U. Bergmann, and S. DeBeer, "X-ray emission spectroscopy evidences a central carbon in the nitrogenase iron-molybdenum cofactor," *Science* **334**(6058), 974–977 (2011).
- <sup>13</sup>U. Bergmann, M. M. Grush, C. R. Horne, P. DeMarois, J. E. Penner-Hahn, C. F. Yocum, D. W. Wright, C. E. Dube, W. H. Armstrong, G. Christou, H. J. Eppley, and S. P. Cramer, "Characterization of the Mn oxidation states in photosystem II by K beta x-ray fluorescence spectroscopy," *J. Phys. Chem. B* **102**(42), 8350–8352 (1998).
- <sup>14</sup>H. Visser, E. Anxolabehere-Mallart, U. Bergmann, P. Glatzel, J. H. Robblee, S. P. Cramer, J. J. Girerd, K. Sauer, M. P. Klein, and V. K. Yachandra, "MnK-edge XANES and K beta XES studies of two Mn-oxo binuclear complexes: Investigation of three different oxidation states relevant to the oxygen-evolving complex of photosystem II," *J. Am. Chem. Soc.* **123**(29), 7031–7039 (2001).
- <sup>15</sup>P. Glatzel, J. Singh, K. O. Kvashnina, and J. A. van Bokhoven, "In situ characterization of the 5d density of states of Pt nanoparticles upon adsorption of CO," *J. Am. Chem. Soc.* **132**(8), 2555 (2010).
- <sup>16</sup>M. A. Beckwith, M. Roemelt, M. N. Collomb, C. DuBoc, T. C. Weng, U. Bergmann, P. Glatzel, F. Neese, and S. DeBeer, "Manganese K beta x-ray emission spectroscopy as a probe of metal-ligand interactions," *Inorg. Chem.* **50**(17), 8397–8409 (2011).
- <sup>17</sup>G. Smolentsev, A. V. Soldatov, J. Messinger, K. Merz, T. Weyhermuller, U. Bergmann, Y. Pushkar, J. Yano, V. K. Yachandra, and P. Glatzel, "X-ray emission spectroscopy to study ligand valence orbitals in Mn coordination complexes," *J. Am. Chem. Soc.* **131**(36), 13161–13167 (2009).
- <sup>18</sup>N. Lee, T. Petrenko, U. Bergmann, F. Neese, and S. DeBeer, "Probing valence orbital composition with iron K beta x-ray emission spectroscopy," *J. Am. Chem. Soc.* **132**(28), 9715–9727 (2010).
- <sup>19</sup>U. Bergmann, C. R. Horne, T. J. Collins, J. M. Workman, and S. P. Cramer, "Chemical dependence of interatomic x-ray transition energies and intensities—A study of Mn K beta" and K beta(2,5) spectra," *Chem. Phys. Lett.* **302**(1–2), 119–124 (1999).
- <sup>20</sup>J. F. Lin, H. Watson, G. Vanko, E. E. Alp, V. B. Prakapenka, P. Dera, V. V. Struzhkin, A. Kubo, J. Y. Zhao, C. McCammon, and W. J. Evans, "Intermediate-spin ferrous iron in lowermost mantle post-perovskite and perovskite," *Nat. Geosci.* **1**(10), 688–691 (2008).
- <sup>21</sup>R. A. Mori, E. Paris, G. Giuli, S. G. Eeckhout, M. Kavcic, M. Zitnik, K. Bucar, L. G. M. Pettersson, and P. Glatzel, "Sulfur-metal orbital hybridization in sulfur-bearing compounds studied by x-ray emission spectroscopy," *Inorg. Chem.* **49**(14), 6468–6473 (2010).
- <sup>22</sup>R. A. Mori, E. Paris, G. Giuli, S. G. Eeckhout, M. Kavcic, M. Zitnik, K. Bucar, L. G. M. Pettersson, and P. Glatzel, "Electronic structure of sulfur studied by x-ray absorption and emission spectroscopy," *Anal. Chem.* **81**(15), 6516–6525 (2009).
- <sup>23</sup>G. Vanko, P. Glatzel, V. T. Pham, R. Abela, D. Grolimund, C. N. Borca, S. L. Johnson, C. J. Milne, and C. Bressler, "Picosecond time-resolved x-ray emission spectroscopy: Ultrafast spin-state determination in an iron complex," *Angew. Chem., Int. Ed.* **49**(34), 5910–5912 (2010).
- <sup>24</sup>H. H. Johann, *Z. Phys.* **69**, 185 (1931).
- <sup>25</sup>T. Johansson, *Z. Phys.* **82**, 507 (1933).
- <sup>26</sup>V. Stojanoff, K. Hamalainen, D. P. Siddons, J. B. Hastings, L. E. Berman, S. Cramer, and G. Smith, "A high-resolution x-ray-fluorescence spectrometer for near-edge absorption studies," *Rev. Sci. Instrum.* **63**(1), 1125–1127 (1992).
- <sup>27</sup>X. Wang, M. M. Grush, A. G. Froeschner, and S. P. Cramer, "High-resolution x-ray fluorescence and excitation spectroscopy of metalloproteins," *J. Synchrotron Radiat.* **4**, 236–242 (1997).
- <sup>28</sup>U. Bergmann and S. P. Cramer, "A high-resolution large-acceptance analyzer for x-ray fluorescence and Raman spectroscopy," *Proc. SPIE* **3448**, 198–209 (1998).
- <sup>29</sup>P. Glatzel, F. M. F. de Groot, and U. Bergmann, "Hard x-ray photon-in photon-out spectroscopy," *Synchrotron Radiat. News* **22**(2), 12–16 (2009).
- <sup>30</sup>I. Llorens, E. Lahera, W. Delnet, O. Proux, A. Brailard, J. L. Hazemann, A. Prat, D. Testemale, F. Gelebart, M. Morand, A. Shukla, N. Bardou, O. Ulrich, S. Arnaud, J. F. Berar, N. Boudet, B. Caillot, P. Chaurand, J. Rose, E. Doelsch, P. Martin, and P. L. Solari, "High energy resolution five-crystal spectrometer for high quality fluorescence and absorption measurements on an x-ray absorption spectroscopy beamline," *Rev. Sci. Instrum.* **83**(6), 9 (2012).
- <sup>31</sup>D. Sokaras, D. Nordlund, T. C. Weng, Alonso-R. Mori, P. Velikov, D. Wagner, A. Garachtchenko, M. George, V. Borzenets, B. Johnson, T. Rabedeau, and U. Bergmann, "A high resolution and large solid angle x-ray Raman spectroscopy end-station at the Stanford Synchrotron Radiation Light-source," *Rev. Sci. Instrum.* **83**(4), 043112 (2012).
- <sup>32</sup>E. Kleymenov, J. A. van Bokhoven, C. David, P. Glatzel, M. Janousch, R. Alonso-Mori, M. Studer, M. Willmann, A. Bergamaschi, B. Henrich, and M. Nachttegaal, "Five-element Johann-type x-ray emission spectrometer with a single-photon-counting pixel detector," *Rev. Sci. Instrum.* **82**(6), 065107 (2011).
- <sup>33</sup>Q. Qian, T. A. Tyson, W. A. Caliebe, and C. C. Kao, "High-efficiency high-energy-resolution spectrometer for inelastic x-ray scattering," *J. Phys. Chem. Solids* **66**(12), 2295–2298 (2005).
- <sup>34</sup>R. Verbeni, M. Kocsis, S. Huotari, M. Krisch, G. Monaco, F. Sette, and G. Vanko, "Advances in crystal analyzers for inelastic x-ray scattering," *J. Phys. Chem. Solids* **66**(12), 2299–2305 (2005).
- <sup>35</sup>P. Glatzel, U. Bergmann, W. W. Gu, H. X. Wang, S. Stepanov, B. S. Mandimutsira, C. G. Riordan, C. P. Horwitz, T. Collins, and S. P. Cramer, "Electronic structure of Ni complexes by x-ray resonance Raman spectroscopy (resonant inelastic x-ray scattering)," *J. Am. Chem. Soc.* **124**(33), 9668–9669 (2002).



- <sup>36</sup>M. Kavcic, M. Zitnik, K. Bucar, A. Mihelic, M. Stuhec, J. Szlachetko, W. Cao, R. A. Mori, and P. Glatzel, "Separation of two-electron photoexcited atomic processes near the inner-shell threshold," *Phys. Rev. Lett.* **102**(14), 143001 (2009).
- <sup>37</sup>B. Dickinson, G. T. Seidler, Z. W. Webb, J. A. Bradley, K. P. Nagle, S. M. Heald, R. A. Gordon, and I. M. Chou, "A short working distance multiple crystal x-ray spectrometer," *Rev. Sci. Instrum.* **79**(12), 123112 (2008).
- <sup>38</sup>L. v. Hamos, "Röntgenspektroskopie und Abbildung mittels gekrümmter kristallreflektoren," *Naturwiss.* **20**, 705–706 (1932).
- <sup>39</sup>J. Hoszowska, and J. C. Dousse, "High-resolution XES and RIXS studies with a von Hamos Bragg crystal spectrometer," *J. Electron Spectrosc. Relat. Phenom.* **137**, 687–690 (2004).
- <sup>40</sup>H. Hayashi, M. Kawata, R. Takeda, Y. Udagawa, Y. Watanabe, T. Takano, S. Nanao, and N. Kawamura, "A multi-crystal spectrometer with a two-dimensional position-sensitive detector and contour maps of resonant K beta emission in Mn compounds," *J. Electron Spectrosc. Relat. Phenom.* **136**(1–2), 191–197 (2004).
- <sup>41</sup>R. Alonso-Mori and P. Glatzel RT4XES; see <https://sites.google.com/site/rt4xes/>
- <sup>42</sup>M. Krisch, Ph.D. dissertation. Dortmund University, 1993.
- <sup>43</sup>S. Takagi, "Dynamical theory of diffraction applicable to crystals with any kind of small distortion," *Acta Crystallogr.* **15**(12), 1311–1312 (1962).
- <sup>44</sup>D. Taupin, "Théorie dynamique de la diffraction des rayons X par les cristaux déformés," *Bull. Soc. Fr. Mineral. Cristallogr.* **87**, 469 (1964).
- <sup>45</sup>S. Hayakawa, A. Yamaguchi, W. Hong, Y. Gohshi, T. Yamamoto, K. Hyashi, J. Kawai, and S. Goto, "A wavelength dispersive x-ray spectrometer for small area x-ray fluorescence spectroscopy at SPring-8 BL39XU," *Spectrochim. Acta, Part B* **54**(171), 171–177 (1999).
- <sup>46</sup>J. Yano, J. Kern, K. D. Irrgang, M. J. Latimer, U. Bergmann, P. Glatzel, Y. Pushkar, J. Biesiadka, B. Loll, K. Sauer, J. Messinger, A. Zouni, and V. K. Yachandra, "X-ray damage to the Mn<sub>4</sub>Ca complex in single crystals of photosystem II: A case study for metalloprotein crystallography," *Proc. Natl. Acad. Sci. U.S.A.* **102**(34), 12047–12052 (2005).
- <sup>47</sup>Y. Mizuno and Y. Ohmura, "Theory of x-ray Raman scattering," *J. Phys. Soc. Jpn.* **22**(2), 445 (1967).
- <sup>48</sup>T. Suzuki, "X-ray Raman scattering experiment. I," *J. Phys. Soc. Jpn.* **22**(5), 1139 (1967).
- <sup>49</sup>W. Schulke, A. Berthold, A. Kaprolat, and H. J. Guntherodt, "Evidence for interlayer band shifts upon lithium Intercalation in graphite from inelastic X-ray-scattering," *Phys. Rev. Lett.* **60**(21), 2217–2220 (1988).
- <sup>50</sup>H. Nagasawa, S. Mourikis, and W. Schulke, "X-ray Raman spectrum of Li, Be, and graphite in a high-resolution inelastic synchrotron x-ray-scattering experiment," *J. Phys. Soc. Jpn.* **58**(2), 710–717 (1989).
- <sup>51</sup>K. Tohji and Y. Udagawa, "X-ray Raman-scattering as a substitute for soft-x-ray-absorption fine-structure," *Phys. Rev. B* **39**(11), 7590–7594 (1989).
- <sup>52</sup>N. Watanabe, H. Hayashi, Y. Udagawa, K. Takeshita, and H. Kawata, "Anisotropy of hexagonal boron nitride core absorption spectra by x-ray Raman spectroscopy," *Appl. Phys. Lett.* **69**(10), 1370–1372 (1996).
- <sup>53</sup>C. Masciovecchio, U. Bergmann, M. Krisch, G. Ruocco, F. Sette, and R. Verbeni, "A perfect crystal x-ray analyser with meV energy resolution," *Nucl. Instrum. Methods Phys. Res. B* **111**(1–2), 181–186 (1996).
- <sup>54</sup>P. A. Montano, D. L. Price, A. T. Macrander, and B. R. Cooper, "Inelastic x-ray scattering from 6H-SiC," *Phys. Rev. B* **66**(16), 165218 (2002).
- <sup>55</sup>B. C. Larson, W. Ku, J. Z. Tischler, C.-C. Lee, O. D. Restrepo, A. G. Eguluz, P. Zschack, and K. D. Finkelstein, "Nonresonant inelastic x-ray scattering and energy-resolved Wannier function investigation of d-d excitations in NiO and CoO," *Phys. Rev. Lett.* **99**(2), 026401 (2007).